Nuclear Engineering and Technology 52 (2020) 2910–2917

Contents lists available at ScienceDirect

Nuclear Engineering and Technology

journal homepage: www.elsevier.com/locate/net

Original Article

Performance of 3D printed plastic scintillators for gamma-ray detection

Dong-geon Kim, Sangmin Lee, Junesic Park, Jaebum Son, Tae Hoon Kim, Yong Hyun Kim, Kihong Pak, Yong Kyun Kim*

Department of Nuclear Engineering, Hanyang University, 222, Wangsimni-ro, Seongdong-gu, Seoul, 04763, South Korea

ARTICLE INFO

Article history:
Received 7 October 2019
Received in revised form
26 May 2020
Accepted 27 May 2020
Available online 6 June 2020

Keywords:
3D printing
Plastic scintillator
Gamma-ray detection
Decay time
Energy resolution
Detection efficiency

ABSTRACT

Digital light processing three-dimensional (3D) printing technique is a powerful tool to rapidly manufacture plastic scintillators of almost any shape or geometric features. In our previous study, the main properties of light output and transmission were analyzed. However, a more detailed study of the other properties is required to develop 3D printed plastic scintillators with expectable and reproducible properties. The 3D printed plastic scintillator displayed an average decay time constants of 15.6 ns, intrinsic energy resolution of 13.2%, and intrinsic detection efficiency of 6.81% for 477 keV Compton electrons from the ^{137}Cs γ-ray source. The 3D printed plastic scintillator showed a similar decay time and intrinsic detection efficiency as that of a commercial plastic scintillator BC408. Furthermore, the presented estimates for the properties showed good agreement with the analyzed data.

1. Introduction

Three-dimensional (3D) printing techniques have been proposed as alternative methods for fabricating radiation detectors because of its advantages of precise shape and dimension control, multi-material capabilities, significant time-saving, and low cost. Gaseous radiation detectors (GRDs) has been developed using the fused deposition modelling (FDM) 3D printing technique for the use of single wire proportional counters (SWPCs) or GEM-based time projection chambers [1]. Geiger-Müller counters can also be manufactured by means of this FDM 3D printing technique with a 3D computer-aided design (CAD) model [2]. Inorganic scintillator YAG:Ce can be fabricated using the stereo photolithography apparatus – laser (SLA) 3D printing technique; the inorganic scintillator has shown 62% light output relative to that of the YAG:Ce single crystal, and 60 ns day time [3]. More recently, this 3D printed YAG:Ce was further researched to improve high-flux laser lighting with higher luminescence, using the Digital Light Processing (DLP) 3D printing technique rather than the conventional dry-pressed method [4]. Plastic scintillators, which are mainly composed of acrylate-based monomers, can be fabricated with the DLP 3D printing technique [5].

Plastic scintillators, which are available in various designs and sizes, have been used in radiation detection systems. Large area plastic scintillators can be used for compensating low intrinsic detection efficiency in expansive radiation detection environments as γ-ray portal monitors [6,7]. In addition, a wide selection of plastic scintillators are available as small diameter fibers. Used either as single fibers or assembled as bundles or ribbons, these scintillating fibers lend themselves to various applications [8–10]. Recently, in radiation therapy, a plastic scintillator was utilized as a dosimeter with very small active volume (less than 0.003 cm^3) to measure the radiation therapy dose with decreasing beam disturbance [11,12]. These plastic scintillators can be fabricated by the following techniques — extrusion, casting, and injection molding that are based on thermal polymerization. In many cases of laboratory-scale research, high-performance plastic scintillators can be fabricated using casting techniques with styrene, polyvinyltoluene, polyvinylcarbazole, and benzylmethacrylate that are known as excellent monomer due to its small band-gap energy [13–15]. A liquid solution with scintillating components is prepared and polymerized at a temperature profile above 100 °C correlated with time for 1–5 days. However, this manufacturing technique is not always efficient. As the material is manufactured with a non-optimized temperature profile, including

* Corresponding author.
E-mail address: ykkim4@hanyang.ac.kr (Y.K. Kim).

https://doi.org/10.1016/j.net.2020.05.030

heating and cooling, air bubbles may be produced inside the material due to internal stress. Furthermore, the resultant product, in many cases, must undergo various finishing processes such as annealing for sustainable performance, cutting to the desired shapes and dimensions, and surface polishing for excellent light transmission to the photodetector.

The DLP 3D printing technique is a powerful tool to rapidly fabricate plastic scintillators of almost any shape or geometric features. However, the first 3D printed plastic scintillator [5] was capable of achieving a low scintillation efficiency of only 28% lower than that of a commercial plastic scintillator EJ204 (Eljen Technology). Various material compositions have been studied to improve the performance of 3D printed plastic scintillators. In the last study, a UV-curable plastic scintillator was developed with a UV LED curing machine for the application to DLP 3D printing. It was confirmed that this scintillator achieved a light output of 34% relative to that of BC408 (Saint-Gobain Crystal), transmittance at 49%, and a fast decay time of 2.46 ns [16]. Recently, a novel plastic scintillator with a new wavelength shifter and intermediate solvent was fabricated using DLP 3D printing; this scintillator demonstrated light output of a 67% relative to that of BC408, and a transmittance of 74% [17]. However, for the application of this 3D printed plastic scintillator to real systems, other properties should be demonstrated as decisive factors. For instance, plastic scintillators with 1–3 ns day time can possibly be used in radiation environments of high-count rates as these scintillators present advantages of reduction in dead time, improvement of timing resolution, and narrower time window for coincidence. For the detection of potential special nuclear materials, radiation portal monitor systems using plastic scintillators with low-cost radiation detection solution require accurate data for energy resolution and intrinsic detection efficiency in fast γ-ray spectroscopy [18]. Moreover, intrinsic energy resolution must be known for the design of complex detection systems using plastic scintillators or for its performance estimates [19,20]. The above-mentioned properties of the 3D printed plastic scintillators have yet to be demonstrated; thus, for the purpose of more predictable and reproducible properties, further research should be performed.

In this research, the 3D printed plastic scintillator was fabricated using DLP 3D printing, based on our previous study [17]. Decay time constants and their contributions were determined by the well-known procedure of convolution fitting with multi-exponential and Gaussian functions. Energy resolution was analyzed in detail with respect to the contributions of the coupled photomultiplier and the scintillator. Based on this energy resolution data, intrinsic detection efficiency was determined using Monte Carlo simulation. For all the above-mentioned properties, the 3D printed and commercial plastic scintillators were compared with each other, and reasonable estimates for the properties were also presented.

2. Experimental setup

2.1. 3D printed plastic scintillator

A plastic scintillator was fabricated using DLP 3D printing, as described in our previous study [17]. Pico2$^{HD\ 37}$ UV DLP 3D printer (ASIGA) [21] was used to fabricate cubic plastic scintillators with dimensions of 30 mm × 30 mm × 10 mm. Fig. 1 shows the concept of the DLP 3D printer. Table 1 shows the resin formulation used in the fabrication of the plastic scintillators.

2.2. Decay time

Scintillation time profile is measured to analyze the decay time of the plastic scintillator; the time profile is determined by the distribution of the time intervals between the start signal of scintillator excitation, and the stop signal of single photon per event. In

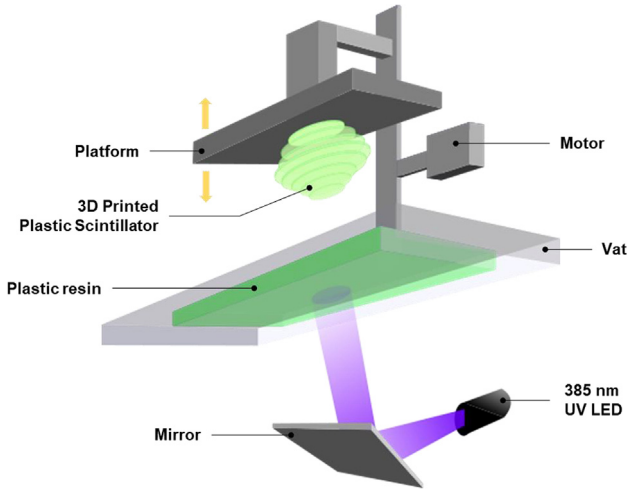

Fig. 1. Concept of Digital Light Processing (DLP) 3D printer.

Table 1
Resin formulation of the 3D printed plastic scintillator.

Types	Names	Ratio*
Primary solvent	BPA(EO)$_{15}$DMA	40%
Secondary solvent	1-methyl-naphthalene	60%
Primary dye	PPO	1.5%
Wavelength shifter	ADS086BE	0.005%
Photoinitiator	TPO	0.03%

* The composition ratio of the materials except the primary and secondary solvents are determined for the total amount of the solvents.

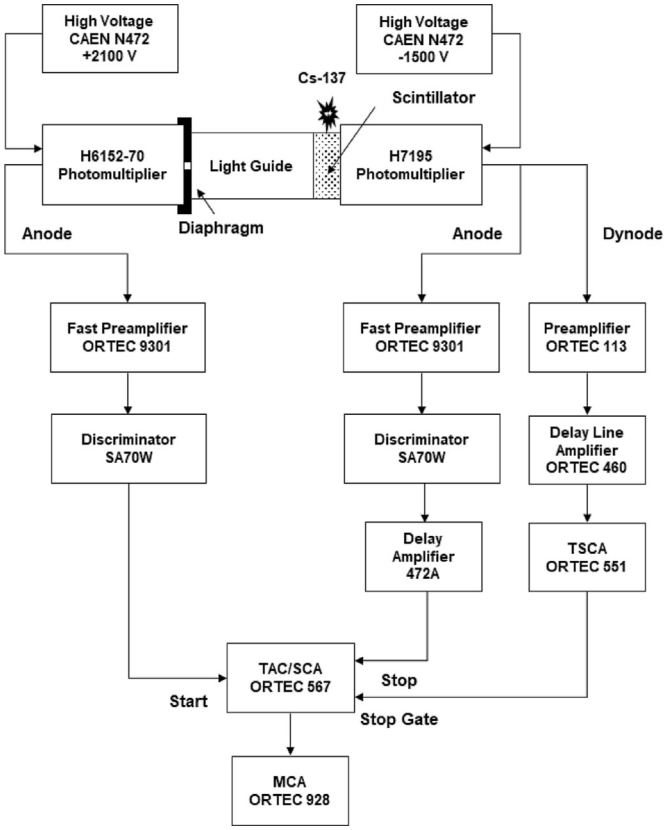

Fig. 2. Schematic of the experimental setup for measuring scintillation time profile of the tested plastic scintillators (BC408 and sample).

this study, the modified experimental setup, which is based on the well-known single photon counting (TCSPC) setup by Thomas-Bollinger method [22], was constructed with reversed, start-stop configuration for the measurement of the scintillation time profile as depicted in Fig. 2. ^{137}Cs γ-ray source was used to generate scintillation excitation, and its radioactivity was 3.93 MBq. The sides of the tested plastic scintillators were wrapped with a Teflon tape to increase the light collection efficiency. The front and back sides of the scintillator were coupled with the photomultiplier (Hamamatsu, H7195) and a light guide (30 mm × 30 mm × 60 mm) using the optical grease BC-630 for optical coupling, respectively. A diaphragm was connected to the light guide, and the hole size of the diaphragm was adjusted to control the average number of incident scintillation photons. The single photons passing through the diaphragm were measured by the photomultiplier (Hamamatsu, H6152-70). This whole setup was placed inside a black box.

When an incident γ-ray of 662 keV from the ^{137}Cs source reacts with the tested scintillator, a number of scintillation photons are generated by a scintillation excitation per event. For the BC408 plastic scintillator that has scintillation light output of 10,000 photons/MeV [23], it can be assumed that the number of scintillation photons per event is on an average approximately 4770 photons, based on the reaction of Compton scattering for maximum energy transfer of 477 keV to Compton electrons. Half of the scintillation photons in the H7195 PMT generate the anode and dynode signals. The anode signal is the start time signal that represents the generation of scintillation excitation, and the dynode signal is the gate signal that involves the deposited energy of the incident γ-ray into the tested scintillator. The other half of the scintillation photons passing through the light guide are incident onto the diaphragm. The hole size of the diaphragm is adjusted to 0.5 mm based on the ratio between the hole area and the light guide area; the diaphragm can accept approximately 0.5 average number of scintillation photons per event. Then, a single photon is incident on the H6152-70 PMT and generates the anode signal that represents the single photon timing signal. The two timing signals from the H7195 PMT and the H6152-70 PMT are discriminated from noise through the fast preamplifier (ORTEC 9301) and the discriminator (SA70W). In this modified system, due to the reversed start-stop sequence, the start timing signal was delayed by Delay Amplifier (ORTEC 472A). The dynode signal from H7195 PMT is amplified by the preamplifier (ORTEC 113) and the amplifier (ORTEC 460). The signal is then filtered only into the signal that involves the deposited energy of maximum energy transfer, 477 keV, of Compton electrons using the window of Timing SCA (TSCA ORTEC 551). In the time-to-amplitude converter (TAC/SCA ORTEC 567), the start and stop signals are reversely recorded when the stop gate signal from the TSCA is accepted. The amplitude of the TAC output signal is determined by the time interval between the start and stop signals. Finally, the multichannel buffer (ORTEC MCB 928) records the distribution of the time intervals by analyzing the amplitude from the TAC.

This modified setup is constrained to accept events only for 477 keV of deposited energy of Compton electrons at the tested scintillator. Furthermore, this setup records the time interval from the reversed start-stop signals. In the TCSPC setups that were based on the typical NIM-TAC module, the signal processing speed became the limiting factor, e.g., pile-up effect, for high count rates in excess of 100 kHz [24]. However, in the reversed start-stop setup, the TAC is started by single photon detection, and stopped by the delayed pulse of scintillation excitation. Consequently, the TAC works only at the rate of single photon detection events, not at the much higher rate of excitation pulse, which leads to more accurate results than the conventional TCSPC setups.

2.3. Energy resolution

A plastic scintillator has a very low photoelectric cross section due to its composition of low atomic number (Z) materials, e.g., carbon and hydrogen; therefore, Compton scattering reaction is almost exclusive. Consequently, it is difficult to analyze energy resolution of plastic scintillators via γ-ray photopeak. G. Dietze et al. [25] presented the γ-γ coincidence technique as a means for studying energy resolution for an organic scintillator composed of low Z materials. This technique allows for selective acquisition of the signals that transfer maximum energy to Compton electrons by γ-rays. From the acquired signals, it is possible to obtain the energy resolution by using the Gaussian function.

In this study, an experimental setup based on γ-γ coincidence technique was constructed. The schematic diagram of the experimental setup for energy resolution measurement of plastic scintillators is depicted in Fig. 3. When an incident γ-ray was reacted with a tested scintillator by Compton scattering, the energy of the

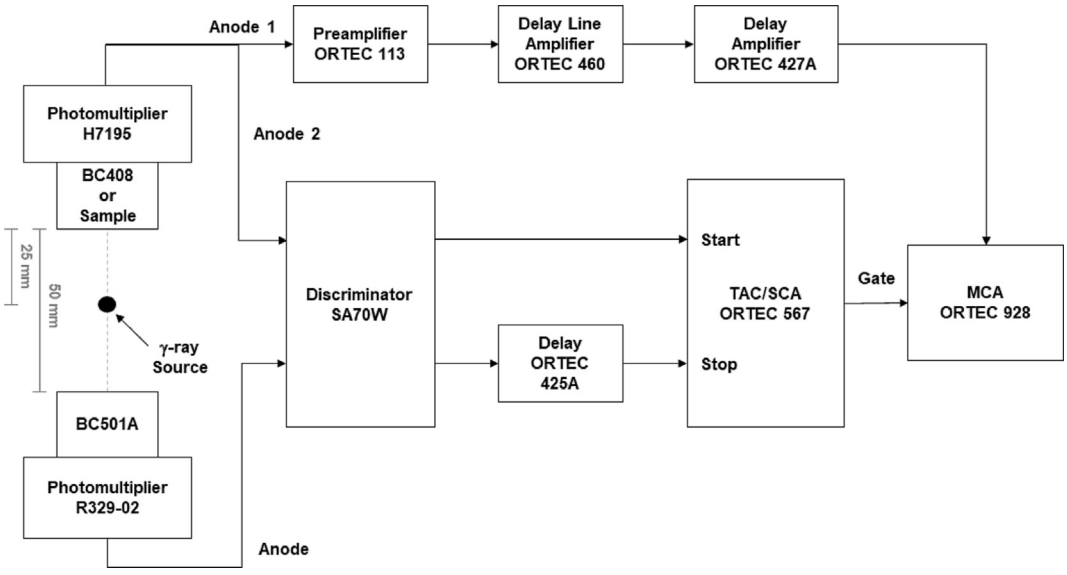

Fig. 3. Schematic of the γ-γ coincidence experimental setup for energy resolution measurement of plastic scintillators.

Table 2
Data of the γ-ray sources used in γ-γ coincidence measurement.

Source	E_γ [keV]	E_c [keV]	E'_γ [keV]	Activity [MBq]
^{137}Cs	662	477	184	3.93
^{54}Mn	835	639	196	7.39
^{60}Co	1170	963	210	2.99
^{60}Co	1330	1120	214	2.99

Compton electron (E_e) is given by

$$E_e = \frac{E_\gamma^2(1-\cos\theta)}{0.511 + E_\gamma(1-\cos\theta)} \quad (1)$$

where E_γ is the energy of the incident γ-ray in unit of MeV. The γ-ray energy (E_γ), Compton edge energy (E_c), and 180° backscattered γ-ray energy (E'_γ) were shown in Table 2 for the γ-ray sources used for γ-γ coincidence measurement. A liquid organic scintillator (Saint-Gobain Crystal, BC501A) with the size of D = 50.8 mm and H = 50.8 mm, which was coupled with the photomultiplier (Hamamatsu, R329-02), was used as a monitor detector. A commercial plastic scintillator BC408 or a sample with the same size was coupled with the photomultiplier (Hamamatsu, H7195), and located at a distance 50 mm from the monitor detector. The γ-ray sources listed in Table 2 were placed halfway at the distance of 50 mm.

In the Compton scattering reaction of an incident γ-ray with the tested scintillator, the anode signals of anode 1 and anode 2 are generated by the deposition of Compton electron (Compton edge, E_c). Then, the γ-ray is backscattered at the 180° angle, and in the reaction of this backscattered γ-ray with the monitor detector, the anode signal is generated. This anode signal and the anode 1 signal from the tested detector are discriminated (SA70W) from noise to provide the start and stop timing signals with a time-to-amplitude converter (TAC/SCA, ORTEC 567), respectively. TAC with a time range of 50 ns provides a gate signal into a multichannel buffer (ORTEC MCB 928), which represents the match of the start and stop signals with an 8 ns delay. When the MCB obtains the gate signal from the TAC, the MCB records the γ-ray energy spectrum with coincidence by obtaining the anode 2 signal that is amplified with the preamplifier (ORTEC 113) and the amplifier (ORTEC 460), and delayed with the module (ORTEC 427A).

2.4. Intrinsic detection efficiency

Intrinsic detection efficiency, which is the probability that an incident γ-ray onto the detector material will react and be detected, can be determined by the integral pulse-height distribution divided by the number of incident γ-rays onto the scintillator. In this study, using Monte Carlo simulation for the detection response function with the empirical resolution data of BC408 and the sample, the pulse-height distribution of the scintillators for ^{137}Cs γ-ray source was simulated. Monte Carlo N-particle eXtend code (MCNPX) 2.7.0. version [26] was used where the pulse height tally (F8 tally option) provides the numerical results of pulses for the energy deposited in the detector for the reactions with γ-rays, such as Rayleigh Thomson scattering (coherent), Compton scattering (incoherent), photoelectric effect, and e^+/e^- pair production. Additionally, FT8 Gaussian Energy Broadening (GEB) card was used to simulate the experimentally observed energy broadening in the detector, e.g., energy resolution, which can be performed by the following formula for the full-width at half maximum (FWHM) with energy.

$$FWHM = a + b\sqrt{E + cE^2} \quad (2)$$

where a, b, c are the fitting parameters.

The simulated pulse height distribution is given as a detection efficiency per a given energy bin, which is normalized to total number of tacking particles, e.g., γ-rays. This detection efficiency is the absolute detection efficiency (ε_{abs}), which is defined as the detection efficiency for all the γ-rays emitted from the source. Intrinsic detection efficiency defined as the detection efficiency for incident γ-rays onto the detector can be calculated by correcting the geometry factor, which is a solid angle ($\Omega/4\pi$) of the detector, to the absolution efficiency. In this simulation, the geometry was the same as that of the experimental setup in Section 2.3 to allow for a comparison between the pulse-height spectra from the experiment and those from the simulation. ^{137}Cs γ-ray isotropic source was located at a distance of 25 mm from the midpoint of the detector's front face, and the size of the detector was 30 mm × 30 mm × 10 mm. The wrapped Teflon tape with 3 mm thickness and the glass window of the H7195 PMT with boronsilicate glass (Pyrex) were modeled for the backscattering effect of γ-rays to the coupled scintillator. A sufficient number of photon particles (10^9) were tracked for statistical uncertainty less than 1%.

3. Results and discussion

The measured scintillation time profiles for BC408 and the sample are shown in Fig. 4. The time profiles were presented with the bin size of 0.93 ns, including the statistical errors. For a very fast scintillator such as a plastic scintillator, it is recommended that a full description of the acquired decay time profile I(t) should consider the combination of light pulse function f(x) with time resolution R(x) [27]. In other words, the acquired time profile I(t) for scintillation light emission can be described with the convolution of multiple exponential function f(x) with time resolution function R(x) of the measurement system as follows:

$$I(t) = f(x)*R(x) = \int_0^\infty f(x)R(t-x)dx \quad (3)$$

The light pulse function f(x) can be described with the sum of multi-exponential components, and an exponential function with three components, which showed the best fit in this research, was adopted as follows:

$$f(x) = \frac{A_1}{\tau_1}e^{-\frac{x}{\tau_1}} + \frac{A_2}{\tau_2}e^{-\frac{x}{\tau_2}} + \frac{A_3}{\tau_3}e^{-\frac{x}{\tau_3}} \quad (4)$$

where τ_1, τ_2, and τ_3 are decay time constants for the light pulse function, and A_1, A_2, and A_3 are the respective contributions of each decay constant. The time resolution function R(x) of the measurement system can be described with a Gaussian distribution with the standard deviation σ. As the uncertainty in the statistical fluctuation of the start timing signal, the standard deviation can be acquired by Gaussian fitting the sharply rising part of the measured time profile. In this study, standard deviations of σ = 1.69 ns and 2.21 ns were obtained for BC408 and the sample, respectively. Given that the time contribution of the reference detector is generally lower and the transit time spread of the H6152-70 PMT detecting single photons is 350 ps at FHWM, it was estimated that the relatively poor standard deviation (σ = 1.7–2.2 ns) is most likely mainly due to the contribution of the light collection process in the long light guide (~60 mm). Accordingly, it is expected that the experimental system without light guide shows better time resolution. Furthermore, the time resolution of the experimental system, including the contribution of the reference detector, can be accurately measured by means of Cherenkov radiation.

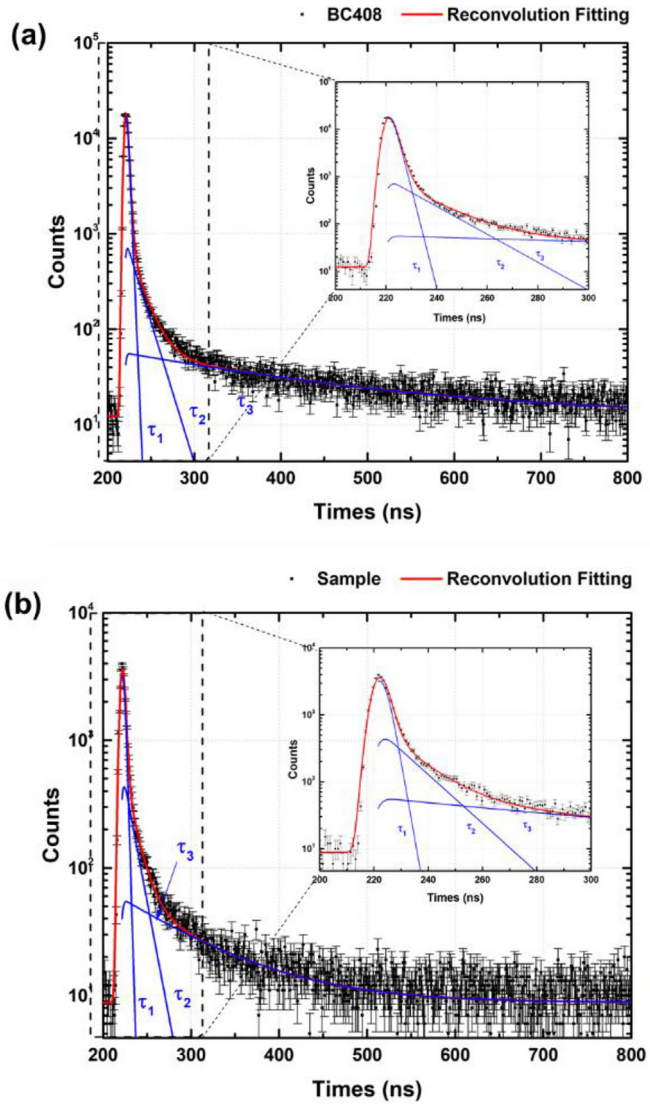

Fig. 4. Measured scintillation decay time profile of (a) BC408 and (b) 3D printed plastic scintillator. The red curves represent the convolution of the scintillation light pulse with time resolution. The blue curves represent the contribution of three decay time components consisting scintillation light pulse. (For interpretation of the references to colour in this figure legend, the reader is referred to the Web version of this article.)

The red curves in Fig. 4 represent the convolution fitting of the sum of the multi exponential function of the three decay components with Gaussian function, and the blue curves represent the analyzed three decay components. The analyzed scintillation decay time constants and contributions are summarized in Table 3. The shortest decay time constant τ_1 of BC408 was 2.07 ± 0.03 ns which was in excellent agreement with the standard of 2.1 ns; this result confirms the good performance of this measurement system. The sample showed superior time properties than those of BC408 for all three decay components The average decay times for BC408 and the sample were 18.3 ns and 15.6 ns, respectively.

Fig. 5 shows the pulse height spectra of γ-γ coincidence, without coincidence, random coincidence, and Gaussian spectrum for BC408 and the sample. Comparing the spectra with/without coincidence, it can be noted that the coincidence spectra for ^{137}Cs and ^{54}Mn γ-rays show a single peak while the coincidence spectra for ^{60}Co γ-rays show two peaks, including contributions from the Compton edge signals. These coincidence spectra, however, also include contributions from random coincidence signals, which need to be removed. The contribution from random coincidence events is mostly due to coincidence events in the tested detector induced by another γ-ray emitted from the source, which can be considered the same as the general Compton spectrum. Consequently, a random coincidence spectrum was sampled from the Compton spectrum, and was subtracted from the coincidence spectrum.

However, despite of this subtraction, the spectrum still includes the signals from Compton scattered γ-rays under angles other than 180° (backscattered γ-rays) due to the geometry of this experiment. These Compton scattered γ-rays can be incident onto the tested scintillator under a certain angle at a distance of 50 mm from the tested detector to the monitor detector. The fraction of the Compton scattered γ-rays incident onto the tested scintillator depending on their angle was calculated by MCNPX Monte Carlo simulation code. This was done under the same conditions as the experiment for BC408 with the ^{137}Cs γ-ray source, while the Cell-Flagging option (CF) in MCNPX code was used for only tagging the Compton scattered γ-rays from the monitor detector onto the tested detector. The fraction of the Compton scattered γ-rays incident onto the scintillator depending on their angle are summarized in Table 4 along with the energies of the scattered γ-rays and the Compton electrons. The fraction of backscattered γ-rays incident onto the tested scintillator at precisely 180° was 16% while the fraction of scattered γ-rays at angles from 180° to 160°, which was correlated to Compton electrons within the energy range E_e = (477.34–473.24) keV, was 72% over the total energy range. The large amount of Compton scattered γ-rays under an angle of 180° can affect the coincidence peak. However, in this experiment, fast measurement was inevitably required at a short distance (50 mm) because 1-methyl-naphthalene, which was used as an intermediate solvent in the sample, has a high volatility, and causes the light output and density of the scintillator without scintillator housing to diminish over time. Accordingly, BC408 also had to be studied under the same conditions for comparison. For a more detailed study in the future, it will be necessary to place the monitor detector at a larger distance or include lead collimator shielding for the backscattered γ-rays at off angles.

The result from the spectrum was fitted with Gaussian function, as shown in Fig. 5. The peak position of the Gaussian spectrum represents the accurate position of the Compton edge for each γ-ray source. Therefore, energy resolutions of BC408 and the sample can be analyzed for the energy of Compton edge for each the sources. Table 5 shows the analyzed results, including the position of Gaussian peak (GP), FWHM, and energy resolution (R) for Gaussian spectrum of BC408 and the 3D printed plastic scintillators, measured with ^{137}Cs, ^{54}Mn, and ^{60}Co γ-ray sources. It was

Table 3
Decay time constants and their contributions of BC408 and the 3D printed plastic scintillators measured in the experimental system.

Plastic scintillator	Decay time constants			Contribution of Decay Components		
	τ_1 (ns)	τ_2 (ns)	τ_3 (ns)	$A_1/\sum A_i$	$A_2/\sum A_i$	$A_3/\sum A_i$
BC408	2.07 ± 0.03	14.7 ± 0.4	215 ± 9	0.821 ± 0.004	0.105 ± 0.002	0.0737 ± 0.0018
Sample	1.90 ± 0.10	11.9 ± 0.7	90.7 ± 5.2	0.661 ± 0.010	0.213 ± 0.008	0.125 ± 0.004

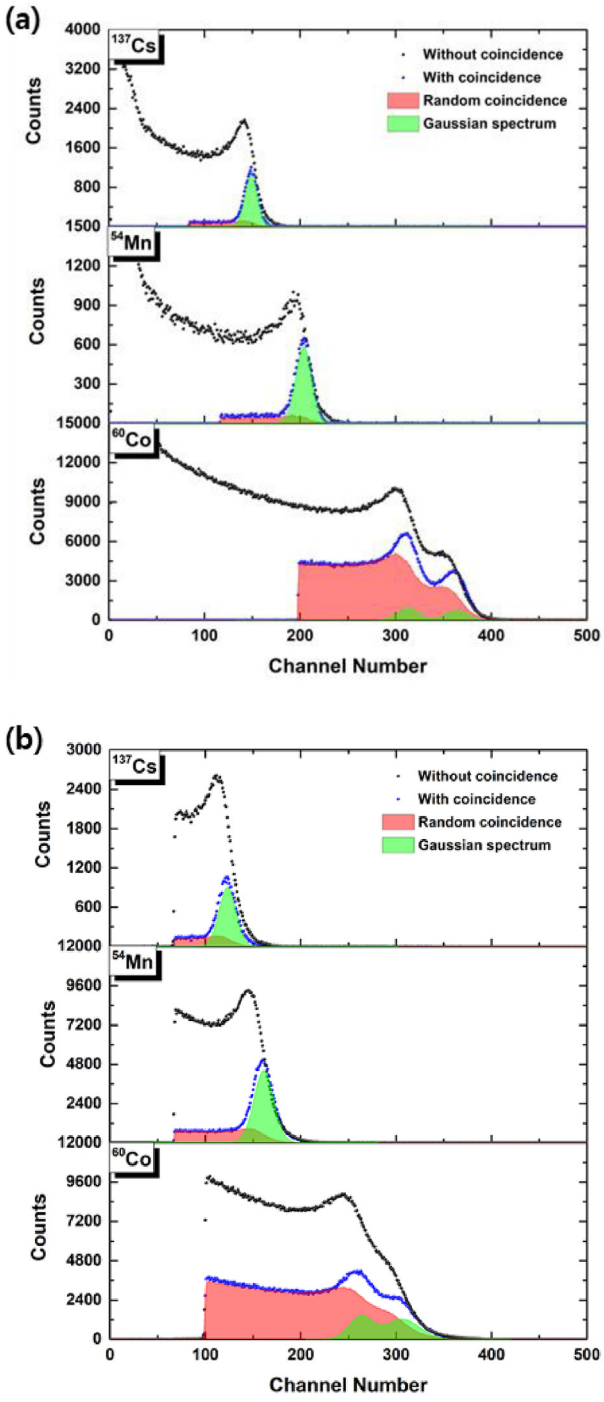

Fig. 5. Compton spectrum without coincidence (dark circle) and with coincidence (blue circle) for (a) commercial plastic scintillator BC408 and (b) the 3D printed plastic scintillator. The smooth lines with shaded region represent random coincidence (red) and Gaussian fitting results for only Compton coincidence (green). (For interpretation of the references to colour in this figure legend, the reader is referred to the Web version of this article.)

confirmed that the two energy resolutions for BC408 and the sample were 9.66 ± 0.04% and 15.4 ± 0.1% for 477 keV of Compton edge energy of the ^{137}Cs source, and the energy resolution decreased with the Compton edge energy.

The energy resolution data was analyzed with an empirical fit as a function of the Compton edge energy for each γ-ray source using the following equation:

$$R(\%) = \sqrt{\alpha^2 + \frac{\beta^2}{E_c} + \frac{\gamma^2}{{E_c}^2}} \quad (5)$$

where α, β, and γ are the fitting parameters: (a) α is a constant term of light transmission from the scintillator to the photocathode of PMT that limits the resolution of the detector system at high energy, (b) β is a stochastic term of light production and attenuation in the scintillator, and of the photon-electron conversion and electron amplification in PMT, and (c) γ is a noise term of dark current in PMT and electronic amplifiers [28]. Fig. 6 shows the empirical fit of energy resolution data for BC408 and the sample. The noise term was expected to be negligible compared to the other two terms, and the energy resolution data were best fitted with parameters $\alpha = 4.22 \pm 1.53\%$, $\beta = 6.09 \pm 0.64\%$, and $\alpha = 6.11 \pm 2.16\%$, $\beta = 9.82 \pm 0.79\%$, for BC408 and the sample, respectively.

The energy resolution (R) of the Gaussian peak, which was measured by γ-γ coincidence with the plastic scintillator coupled with the photomultiplier, can be written as $R^2 = {R_{tot}}^2 = {R_{sc}}^2 + {\delta_{tr}}^2 + {\delta_p}^2$ where R_{sc} is the intrinsic energy resolution that is the contribution of the scintillator associated with the fluctuation of the scintillation light output induced by the non-proportional response of γ-ray within the scintillator, δ_{tr} is the transfer resolution that is associated with the probability that a photon from the scintillator results in the arrival of photoelectrons at the first dynode, and δ_p is the amplification resolution of the photomultiplier induced by its gain variance [29]. In the modern scintillation detectors, the transfer component is negligible compared to other contributions of the energy resolution, and in the case of small δ_{tr}, the above-mentioned equation that can be transformed and written as

$${R_{tot}}^2 = {R_{sc}}^2 + {R_{pmt}}^2 \quad (6)$$

P. Dorenbos et al. presented the definition of R_{pmt}, assuming the gain variance in the number of photoelectrons generated from the photocathode of the photomultiplier follows Poisson statistics: $R_{pmt} = 2.355\sqrt{\frac{1+\nu(M)}{N_{phe}}}$, where ν(M) is the gain variance in the photomultiplier and N_{phe} is photoelectron yield (phe/MeV). The equation for gain variance is $\nu(M) = \frac{1}{\bar{R}-1}$, where $\bar{R}$ is gain of the average dynode with the applied voltage of the photomultiplier [30]. In this study, $\bar{R}$ was 3.15 at the applied voltage of −1500 V of the H7195 photomultiplier. N_{phe} was calculated by multiplying the absolute light output N_{ph} with effective quantum efficiency $Q.E._{eff}$ for the scintillator; these two parameters were measured in our previous study [17].

The above-mentioned parameters are presented in Table 6. The intrinsic energy resolutions of BC408 and the sample were presented for 477 keV Compton electrons from the ^{137}Cs γ-ray source, with values of 7.76% and 13.2%, respectively. The intrinsic energy resolution of the BC408 plastic scintillator was in good agreement (within 5% error) with that found by Ł. Świderski et al. [32]. It should be noted that the intrinsic resolution is mainly related to the non-proportional response of the scintillator. This characteristic has been regarded as the fundamental limitation to the achievable

Table 4
The fraction of the Compton scattered γ-rays incident onto the tested plastic scintillator BC408 over the total energy range under certain angles (θ), along with their energy (E_γ) and the Compton electron energy (E_e).

Angle	180°	180° ≦ θ ≦ 175°	180° ≦ θ ≦ 170°	180° ≦ θ ≦ 160°
E_e (keV)	477.34	477.08	476.32	473.24
E_γ (keV)	184.32	184.58	185.34	188.42
Fraction	16%	54%	65%	72%

Table 5
The position of Gaussian peak (GP), FWHM, and energy resolution (R) for Gaussian spectrum of plastic scintillators, measured with ^{137}Cs, ^{54}Mn, and ^{60}Co γ-ray sources.

Source	Compton edge energy E_c [keV]	BC408			Sample		
		GP channel	FWHM [ch]	Resolution [%]	GP channel	FWHM [ch]	Resolution [%]
^{137}Cs	477	149 ± 0.03	15.6 ± 0.1	9.66 ± 0.04	123 ± 0.05	21.0 ± 0.1	15.4 ± 0.1
^{54}Mn	639	204 ± 0.1	19.5 ± 0.1	9.02 ± 0.05	161 ± 0.06	24.3 ± 0.2	13.9 ± 0.1
^{60}Co	963	315 ± 0.1	24.3 ± 0.3	7.42 ± 0.08	264 ± 0.24	30.7 ± 0.7	11.1 ± 0.2
^{60}Co	1120	366 ± 0.1	26.0 ± 0.3	6.88 ± 0.09	307 ± 0.30	36.0 ± 1.0	11.3 ± 0.3

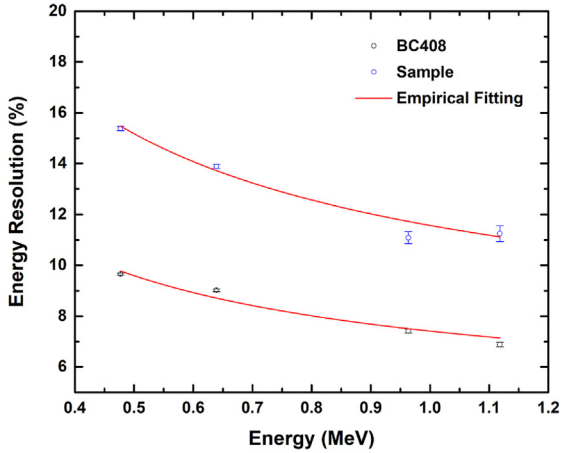

Fig. 6. Empirical fit for energy resolution data of BC408 and 3D printed plastic scintillator.

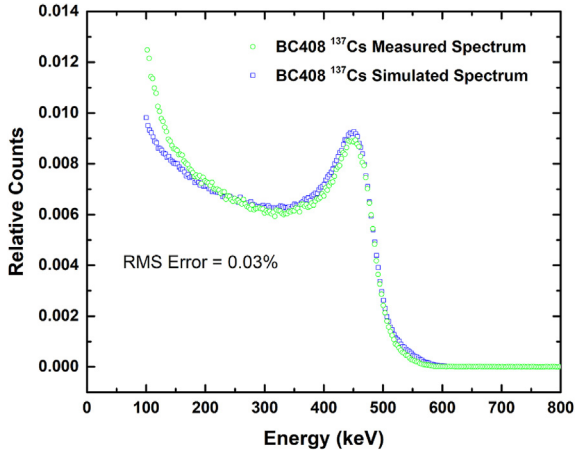

Fig. 7. Normalized results for measured and simulated energy spectrum of BC408 for ^{137}Cs γ-ray source.

resolution in scintillators, and the characteristics of non-proportionality for organic scintillators have been studied by A. Nassalski et al. [33] and Ł. Świderski et al. [32]. They reported that the organic scintillators BC408 and BC501A exhibit non-proportionality in the range from 10 keV to 4 MeV. The reasons for this non-proportionality have not been described clearly. However, for the development of new and improved organic scintillators with enhanced energy resolution, different organic scintillators need to be studied and their experimental data should be gathered.

Fig. 7 shows a comparison between the ^{137}Cs γ-ray energy spectra of BC408 plastic scintillator from the experiment, and the MCNPX simulation with the empirical data of the energy resolution. The experimentally measured energy spectrum was obtained from the pulse height spectrum by linear calibration from channel number to energy. The fitting parameters used in the MCNPX simulation were 0 MeV, 0.612 $MeV^{1/2}$, and 0.464 MeV^{-1} for BC408, and 0 MeV, 0.0982 $MeV^{1/2}$, 0.387 MeV^{-1} for the sample. The relative errors for the results were represented by the Root Mean Square (RMS) above 100 keV as plastic scintillators are mainly used above 100 keV. It was noted that the RMS between the energy spectra from the experiment, and the simulation was 0.03%, thereby verifying the simulated results. The absolute detection efficiencies (ε_{abs}) of BC408 and the sample were calculated by summing the efficiencies of the simulated energy spectrum above 100 keV, which were converted to the intrinsic detection efficiencies (ε_{int}) by multiplying the solid angle of the detector. It was found that the intrinsic detection efficiencies of BC408 and the sample were 6.85% and 6.81% for ^{137}Cs γ-ray source, respectively.

These results can be estimated from the ratio between total linear attenuation coefficients for the material compositions of BC408 and the sample because the intrinsic detection efficiency of the plastic scintillator for γ-rays is correlated with its atomic electron density. It is known that the main elements of BC408 plastic scintillator is carbon and hydrogen [23], and those of the sample were reported in Ref. 17. The data of mass attenuation coefficient for these elements were used from the National Institute of Standards and Technology (NIST) [34]. The ratio of total linear

Table 7
The weight ratio (w_i) for the elements, density (ρ), and total linear attenuation coefficient (μ) of BC408 and the sample.

Plastic scintillators	Weight ratio[a]					Density, ρ [g/cm^3]	μ[b] [cm^{-1}]
	H (w_1)	C (w_2)	N (w_3)	O (w_4)	P (w_5)		
BC408	0.084	0.916	–	–	–	1.023 ± 0.001	0.0859
Sample	0.072	0.832	8.81E-04	0.096	2.47E-05	1.038 ± 0.001	0.0863

[a] The weight ratio of the sample can be found in Ref. 17.
[b] Total linear attenuation coefficient was calculated by the following equation. $\mu = \sum\left(w_i \times \left(\frac{\mu}{\rho}\right)_i\right) \times \rho$

Table 6
Average dynode's gain ($\overline{R}$), gain variance ν(M), absolute light output (N_{ph}), effective quantum efficiency ($Q.E._{eff}$), photoelectron yield (N_{phe}), total energy resolution (R_{tot}), amplification resolution of the photomultiplier (R_{pmt}), and intrinsic energy resolution (R_{sc}).

Plastic scintillator	$\overline{R}$	ν(M)	N_{ph}* (ph/MeV)	$Q.E._{eff}$*	N_{phe} (phe/MeV)	R_{tot} (%)	R_{pmt} (%)	R_{sc} (%)
BC408	3.15	0.466	10,500 ± 300	0.235 ± 0.001	2470 ± 70	9.66 ± 0.04	5.74 ± 0.08	7.76 ± 0.08
Sample	3.15	0.466	7000 ± 400	0.188 ± 0.001	1320 ± 80	15.4 ± 0.1	7.86 ± 0.23	13.2 ± 0.18

* The measurements of absolute light output and effective quantum efficiency of Ref. [17] was used, and the experimental error of N_{ph} in Ref. [31] was used for the error estimation of N_{phe}, R_{pmt}, and R_{sc}.

attenuation coefficients was compared with that of intrinsic detection efficiencies for BC408 and the sample for 662 keV γ-ray from ^{137}Cs source. Table 7 shows the weight ratio for the elements, density, and total linear attenuation coefficients of BC408 and the sample. The ratio of total linear attenuation coefficients was 1.00, similar to the ratio of 1.01 of intrinsic detection efficiencies.

4. Conclusions

For the properties of decay time, energy resolution, and intrinsic detection efficiency, data was presented and compared between the 3D printed plastic scintillator and the commercial plastic scintillator, BC408. The 3D printed plastic scintillator was composed of the resin formulation developed in our previous study [17]. This 3D printed plastic scintillator, which had similar decay time and intrinsic detection efficiency as those of BC408, can be used in fast timing detection or in environments with high count rates. Compared to the data for intrinsic detection efficiency of the sample, the estimates were in good agreement within reasonable error margins. Furthermore, it is expected that the collected intrinsic energy resolution data of the sample can be used as a reference for the development of new plastic scintillators using the 3D printing technique.

For further research on improvement of 3D printed plastic scintillator, the focus should be on the resin recipe. 1-methylnaphthalene was used as an intermediate solvent in this study, whose high volatility causes light output and density of the scintillator without scintillator housing to diminish over time. It was found that styrene-based 3D printed plastic scintillator also has volatility, this disadvantage can be overcome by only the use of excellent acrylic monomer with more benzene rings per molecule. Meanwhile, it is possible to improve the performance of the 3D printed plastic scintillator by the use of a fluorescent dye with high Z material, which leads to the 3D printed scintillator with high density and high detection efficiency to γ-ray.

Notes

The authors declare no competing financial interest.

Acknowledgement

This work was supported by the National Research Foundation of Korea (NRF) grant funded by the Ministry of Science and ICT (No. NRF-2016M2A2A6A03912636).

References

[1] S. Fargher, C. Steer, L. Thompson, The use of 3D printing in the development of gaseous radiation detectors, in: Advancements in Nuclear Instrumentation Measurement Methods and Their Applications, Liege, Belgium, June 19-23, 2017.
[2] 3D printing industry. https://3dprintingindustry.com/news/teen-nuclear-physicist-builds-geiger-counter-with-3d-printed-parts-53696/.
[3] G.A. Dosovitskiy, P.V. Karpyuk, P.V. Evdokimov, D.E. Kuznetsova, V.A. Mechinsky, A.E. Borisevich, A.A. Fedorov, V.I. Putlayev, A.E. Dosovitskiy, M.V. Korjik, First 3D-printed complex inorganic polycrystalline scintillator, CrystEngComm 19 (2017) 4260–4264, https://doi.org/10.1039/c7ce00541e.
[4] S. Hu, Y. Liu, Y. Zhang, Z. Xue, Z. Wang, G. Zhou, C. Lu, H. Li, S. Wang, 3D printed ceramic phosphor and the photoluminescence property under blue laser excitation, J. Eur. Ceram. Soc. 39 (2019) 2731–2738, https://doi.org/10.1016/j.jeurceramsoc.2019.03.005.
[5] Y. Mishnayot, M. Layani, I. Cooperstein, S. Magdassi, G. Ron, Three-dimensional printing of scintillating materials, Rev. Sci. Instrum. 85 (2014), 085102, https://doi.org/10.1063/1.4891703.
[6] B.D. Geelhood, J.H. Ely, R.R. Hansen, R.T. Kouzes, J.E. Schweppe, R.A. Warner, Overview of portal monitoring at border crossings, in: IEEE Nuclear Science Symposium, Medical Imaging Conference, Oregon, U.S.A, 2003. October 20-24.
[7] V.N. Bliznyuk, A.F. Seliman, A.A. Ishchenko, N.A. Derevyanko, T.A. Devol, New efficient organic scintillators derived from pyrazoline, ACS Appl. Mater. Interfaces 8 (2016) 12843–12851, https://doi.org/10.1021/acsami.6b02719.
[8] G.F. Knoll, Radiation Detection and Measurement, John Wiley & Sons, New York, 2010.
[9] M. Atac, J. Park, D. Cline, D. Chrisman, M. Petroff, E. Anderson, Scintillating fiber tracking for the SSC using visible light photon counters, Nucl. Instrum. Methods Phys. Res. A. 314 (1992) 56–62, https://doi.org/10.1016/0168-9002(92)90498-S.
[10] M.D. Petroff, M. Attac, High energy particle tracking using scintillating fibers and solid state photomultiplier, IEEE Trans. Nucl. Sci. 36 (1989) 163–164, doi: ieeexplore.ieee.org/document/34425.
[11] P. Carrasco, N. Jornet, O. Jordi, M. Lizondo, A. Latorre-Musoll, T. Eudaldo, A. Ruiz, M. Ribas, Characterization of the Exradin W1 scintillator for use in radiotherapy, Med. Phys. 42 (2015) 297–304, https://doi.org/10.1118/1.4903757.
[12] T.S.A. Underwood, B.C. Rowland, R. Ferrand, L. Vieillevigne, Application of the Exradin W1 scintillator to determine Ediode 60017 and microDiamond 60019 correction factors for relative dosimetry within small MV and FFF fields, Phys. Med. Biol. 60 (2015) 6669–6683, https://doi.org/10.1088/0031-9155/60/17/6669.
[13] S.W. Moser, W.F. Harder, C.R. Hurlbut, M.R. Kusner, Principles and practice of plastic scintillator design, Radiat. Phys. Chem. 41 (1993) 31–36, https://doi.org/10.1016/0969-806X(93)90039-W.
[14] A. Pla-Dalmau, A.D. Bross, K.L. Mellott, Low-cost extruded plastic scintillator, Nucl. Instruments Methods Phys. Res. Sect. A Accel. Spectrometers, Detect. Assoc. Equip. 466 (2001) 482–491, https://doi.org/10.1016/S0168-9002(01)00177-2.
[15] C.H. Lee, J. Son, T.H. Kim, Y.K. Kim, Characteristics of plastic scintillators fabricated by a polymerization reaction, Nucl. Eng. Technol. 49 (2017) 592–597, https://doi.org/10.1016/j.net.2016.10.001.
[16] S. Lee, J. Son, D.G. Kim, J. Choi, Y.K. Kim, Characterization of plastic scintillator fabricated by UV LED curing machine, Nucl. Instruments Methods Phys. Res. Sect. A Accel. Spectrometers, Detect. Assoc. Equip. 929 (2019) 23–28, https://doi.org/10.1016/j.nima.2019.03.048.
[17] J. Son, D.G. Kim, S. Lee, J. Park, Y. Kim, T. Schaarschmidt, Y.K. Kim, Improved 3D printing plastic scintillator fabrication, J. Kor. Phys. Soc. 73 (2018) 887–892, https://doi.org/10.3938/jkps.73.887.
[18] M. Hamel, C. Dehe-Pittance, R. Coulon, F. Carrel, P. Pillot, E. Barat, T. Dautremer, T. Montagu, S. Normand, Gammastic: towards a pseudo-gamma spectrometry in plastic scintillators, in: Advancements in Nuclear Instrumentation Measurement Methods and Their Applications, Marseille, France, June 23-27, 2013.
[19] A. Moiseev, E. Ferrara, R. Ojha, A. Smith, E. Hays, J.W. Mitchell, J. McEnery, J. Perkins, J. Racusin, D. Thompson, J. Buckley, R. Caputo, M. Ajello, D.H. Hartmann, Extending fermi LAT discoveries: Compton-pair production space telescope (ComPair) for MeV gamma-ray astronomy, in: International Cosmic Ray Conference, Hague, Netherlands, July 30 to August 6, 2015.
[20] K. Roemer, G. Pausch, C.M. Herbach, Y. Kong, R. Lentering, C. Plettner, J. Stein, M. Moszyński, Ł. Swiderski, T. Szczęśniak, A technique for measuring the energy resolution of low-Z scintillators, IEEE Nucl. Sci. Symp. Conf. Rec. (2009) 6–11, https://doi.org/10.1109/NSSMIC.2009.5401909.
[21] ASIGA. https://www.asiga.com.
[22] L.M. Bollinger, G.E. Thomas, Measurement of the time dependence of scintillation intensity by a delayed-coincidence method, Rev. Sci. Instrum. 32 (1961) 1044–1050, https://doi.org/10.1063/1.1717610.
[23] Saint gobain crystal. https://www.crystals.saint-gobain.com.
[24] W. Becker, Advanced Time-Correlated Single Photon Counting Techniques, Springer, Berlin, 2005.
[25] G. Dietze, Energy calibration OF NE-213 scintillation counters BY gamma-rays, IEEE Trans. Nucl. Sci. 26 (1) (1979) 398–402, https://doi.org/10.1109/TNS.1979.4329665.
[26] D.B. Pelowitz, MCNPX™ USER'S MANUAL 2.7.0 Version, Los Alamos Natl. Lab., 2011, pp. 1–645. LA-CP-05-0369.
[27] T.M. Undagoitia, F.V. Feilitzsch, L. Oberauer, W. Potzel, A. Ulrich, J. Winter, M. Wurm, Fluorescence decay-time constants in organic liquid scintillators, Rev. Sci. Instrum. 80 (2009), 043301, https://doi.org/10.1063/1.3112609.
[28] G. Dietze, H. Klein, Gamma-calibration of NE 213 scintillation counters, Nucl. Instrum. Methods 193 (1982) 549–556, https://doi.org/10.1016/0029-554X(82)90249-X.
[29] P. Dorenbos, J.T.D. de Haas, C.W.V. van Eijk, Non-proportionality in the scintillation response and the energy resolution obtainable with scintillation crystals, IEEE Trans. Nucl. Sci. 42 (1995) 2190–2202, https://doi.org/10.1109/23.489415.
[30] J.B. Birks, The Theory and Practice of Scintillation Counting, Pergamon Press, 1964.
[31] D.G. Kim, J. Park, J. Son, S. Lee, S.J. Seon, J.Y. Jeong, Y.K. Kim, Light output analysis of 3D printed plastic scintillator, in: Transaction of the Korean Nuclear Society Autumn Meeting, Yeosu, Korea, October 25-26, 2018.
[32] Ł. Świderski, R. Marcinkowski, M. Moszynski, W. Czarnacki, M. Szawlowski, T. Szczesniak, G. Pausch, C. Plettner, K. Roemer, Electron response of some low-Z scintillators in wide energy range, J. Instrum. 7 (2012) P06011, https://doi.org/10.1088/1748-0221/7/06/P06011.
[33] A. Nassalski, M. Moszyński, A. Syntfeld-Każuch, Ł. Świderski, T. Szczęśniak, Non-proportionality of organic scintillators and BGO, IEEE Trans. Nucl. Sci. 55 (3) (2008) 1069–1072, https://doi.org/10.1109/TNS.2008.2012282.
[34] NIST. https://www.nist.gov.